ChemSusChem

Research Article
doi.org/10.1002/cssc.202301607

Chemistry Europe
European Chemical Societies Publishing

www.chemsuschem.org

Self-etching assembly of designed NiFeMOF nanosheet arrays as high-efficient oxygen evolution electrocatalyst for water splitting

Shifan Zhang,[a] Miao Liao,[a] Zhiyang Huang,[a] Mingcheng Gao,[a] Xinqiang Liu,[a] Haoran Yin,[a] Tayirjan Taylor Isimjan,*[c] Dandan Cai,*[b] and Xiulin Yang*[a]

2D metal-organic frameworks (MOFs) have emerged as potential candidates for electrocatalytic oxygen evolution reactions (OER) due to their inherent properties like abundant coordination unsaturated active sites and efficient charge transfer. Herein, a versatile and massively synthesizable self-etching assembly strategy wherein nickel–iron foam (NFF) acts as a substrate and a metal ion source. Specifically, by etching the nickel–iron foam (NFF) surface using ligands and solvents, Ni/Fe metal ions are activated and subsequently reacted under hydrothermal conditions, resulting in the formation of self-supporting nanosheet arrays, eliminating the need for external metal salts. The obtained 33% NiFeMOF/NFF exhibits remarkable OER performance with ultra-low overpotentials of 188/231 mV at 10/100 mA cm^{-2}, respectively, outperforming most recently reported catalysts. Besides, the built 33% NiFeMOF/NFF$^{(+)}$||Pt/C$^{(-)}$ electrolyzer presents low cell voltages of 1.55/1.83 V at 10/100 mA cm^{-2}, superior to the benchmark $RuO_2^{(+)}$||Pt/C$^{(-)}$, implying good industrialization prospects. The excellent catalytic activity stems from the modulation of the electronic spin state of the Ni active site by the introduction of Fe, which facilitates the adsorption process of oxygen-containing intermediates and thus enhances the OER activity. This innovative approach offers a promising pathway for commercial-scale sustainable energy solutions.

1. Introduction

The oxygen evolution reaction (OER) is crucial in a range of electrochemical energy storage and conversion applications, such as rechargeable metal–air batteries, water splitting powered by solar or electricity, and regenerative fuel cells.[1] However, since the OER process involves the formation of O–O bonds and a four-proton-coupled electron transfer, it often exhibits sluggish kinetics, thus limiting the efficiency of electrochemical systems.[2] Therefore, it is essential to develop efficient OER electrocatalysts to accelerate the reaction kinetics and improve electrocatalytic efficiency. Although precious metal oxides like IrO_2 and RuO_2 are considered benchmark OER electrocatalysts,[3] their significant costs, limited durability, and rarity restrict their broad commercial use.[4] Consequently, there is an urgent need to develop low-cost, highly active, durable, and abundant non-noble metal catalysts for OER.[5]

Two-dimensional (2D) metal-organic framework (MOF) nanosheets are regarded as potential OER electrocatalysts due to their efficient electron transport, rapid mass transfer rate, and abundant coordination unsaturated active sites.[6] However, most reported MOFs have been in powder form, so binders must be used to fabricate working electrodes, which results in partial active sites being covered.[7] To address this, the direct growth of 2D MOF nanosheets on conductive substrates (nickel–iron foam (NFF), nickel foam (NF), iron foam (IF), and carbon cloth (CC), etc.) has been explored to develop in-situ assembled electrodes.[8] A challenge that arises, however, is the weak adhesive force between MOFs and these substrates, which complicates the growth process. Metal foams, particularly, have emerged as attractive carriers owing to their superior electrical conductivity, flexibility, and unique microporous channels.[9] Yet, the prevailing research often pigeonholes them as mere support materials, ignoring their intrinsic properties. Hence, we propose an innovative self-etching assembly strategy that utilizes NFF as the support material and metal source. This strategy forgoes the need for external metal salt additions during MOF synthesis. Instead, the NFF undergoes oxidation, releasing metal cations due to the etching effect of ligands and solvents. This not only slashes the catalyst preparation costs but also paves the way for an easier large-scale synthesis.

In this study, we introduce a straightforward and adaptable self-etching assembly method to create 2D NiFeMOF nanosheets on nickel–iron foam (NiFeMOF/NFF), serving as effective and durable OER electrocatalysts. Impressively, the optimized

[a] S. Zhang, M. Liao, Z. Huang, M. Gao, X. Liu, H. Yin, Prof. Dr. X. Yang
Guangxi Key Laboratory of Low Carbon Energy Materials
School of Chemistry and Pharmaceutical Sciences
Guangxi Normal University
Guilin 541004, China
E-mail: xlyang@gxnu.edu.cn

[b] Dr. D. Cai
School of Chemical Engineering and Technology
Sun Yat-sen University
Zhuhai, 519082, China
E-mail: caidandan86@163.com

[c] Dr. T. T. Isimjan
Saudi Arabia Basic Industries Corporation (SABIC) at King Abdullah University of Science and Technology (KAUST)
Thuwal 23955-6900, Saudi Arabia
E-mail: isimjant@sabic.com

Supporting information for this article is available on the WWW under https://doi.org/10.1002/cssc.202301607

33% NiFeMOF/NFF composite showcases exceptional OER performance with ultra-low overpotentials (188 V@10 mA cm^{-2} and 240 V@100 mA cm^{-2}) and a smaller Tafel slope (31 mV dec^{-1}). Crucially, it maintains a consistent overpotential, even after 100 h of uninterrupted activity at both 10 and 100 mA cm^{-2}. In a dual-electrode setup (33% NiFeMOF/NFF$^{(+)}$||Pt/C$^{(-)}$), it demands just 1.55 and 1.83 V to achieve 10 and 100 mA cm^{-2}, respectively, demonstrating impressive long-term durability at 100 mA cm^{-2} for a span of 100 h. The exceptional electrocatalytic performance of the 33% NiFeMOF/NFF arises from its evenly interlinked nanosheet architecture and the cooperative interplay between the Ni and Fe elements. This research, thus, offers an exciting avenue for crafting cost-effective, high-performing metal-based MOF catalysts suited for sustainable energy conversion technologies.

Experimental section

Preparation of NiFeMOF/NFF

In a typical process, H_2NDC (50 mg) was dissolved in a blend of DMF (2 mL), ethanol (2 mL), and water (2 mL) within a 25 mL Teflon-lined container. This mixture was sonicated for 15 minutes until a uniform solution was achieved. An NFF (NiFe ratio is about 3:7, purchased from Guangshengjia New Material Co.) piece measuring 2 cm×1 cm×0.5 mm was then submerged in this solution. The sealed vessel was relocated to a reactor and maintained at 120 °C for a period of 24 h. After the temperature returned to ambient, the metal foam was extracted, rinsed multiple times with ethanol, and subjected to vacuum drying at 60 °C for the night. The resultant product was termed 33% NiFeMOF/NFF, reflecting the ethanol percentage used. To investigate the effect of ethanol concentration on the structure and catalytic efficiency, additional tests were performed at a fixed solution volume of 6 mL with an H_2O to DMF ratio of 1:1. The tests were performed at 0%, 17%, 50%, and 67% ethanol concentrations. The resulting samples were correspondingly designated as 0% NiFeMOF/NFF, 17% NiFeMOF/NFF, 50% NiFeMOF/NFF, and 67% NiFeMOF/NFF.

Synthesis of NiMOF/NF and FeMOF/IF

For comparison, the preparation process is the same as 33% NiFeMOF/NFF, except that NFF was replaced with NF and IF, respectively.

Material characterizations

Morphology and structure were characterized by field emission scanning electron microscopy (FE-SEM; FEI Quanta 200, FEI, Eindhoven, Holland), transmission electron microscopy and high-resolution transmission electron microscopy (TEM and HRTEM; Thermo Fisher Scientific, America). X-ray diffraction (XRD) patterns were obtained by a Rigaku D/Max-3c instrument. X-ray photoelectron spectroscopy (XPS, Thermo Fischer ESCALAB 250 Xi) and Al Kα radiation analyzed surface compositions and valence states. All XPS spectra were calibrated by shifting the detected critical carbon C 1s peak to 284.8 eV. The thickness of catalyst was tested using an AFM (Dimension ICON, Bruker, America).

Electrochemical measurements

All electrochemical measurements were carried out using the Multi-channel electrochemical workstation (Bio-logic VMP3, France) with a typical three-electrode system in 1.0 M KOH solution. The as-prepared catalyst, carbon rod and Hg/HgO electrode were used as the working electrode, counter electrode and reference electrode, respectively. Linear sweep voltammetry (LSV) was performed at a scan rate of 0.5 mV s^{-1} in the range of 1.2–1.8 V (*vs.* RHE), and the *iR*-drop (95%) correction was applied to all the polarization curves. The measured potentials were converted to the RHE scale using the Nernst equation: E (*vs.* RHE) = E (*vs.* Hg/HgO) + 0.059×pH + 0.098 V. The Tafel slope was determined from $\eta = a + b \times \log j$, where η represents the overpotential, a is a constant, b refers to the Tafel slope, and j stands for the current density. Electrochemical impedance spectroscopy (EIS) was performed with a 5 mV amplitude in a frequency range from 100 kHz to 10 mHz at a potential of 1.48 V (*vs.* RHE). The EIS data were fitted using ZSimDemo software. The electrochemical surface area (ECSA) was determined by the double-layer capacitance (C_{dl}). The C_{dl} of the electrode was characterized by cyclic voltammetry (CV) with various scan rates of 10, 20, 30, 40, and 50 mV s^{-1} at the non-Faradic region within the potential range from 1.1 V to 1.2 V (*vs.* RHE). The formula for calculating C_{dl} is: $C_{dl} = (j_a - j_c)/(2 \times \nu)$, where j_a and j_c correspond to the anodic and cathodic current density, respectively, and ν represents the scanning rate. The ECSA of catalyst was calculated using the expression: $A_{ECSA} = C_{dl}/C_s$, where the value of C_s is generally in the range of 20 to 60 μF cm^{-2}. An average value of C_s was 40 μF cm^{-2}. The stability of samples was measured by chronopotentiometry at a current density of 100 mA cm^{-2} for an extended time period. The overall water splitting was measured employing a two-electrode system with a voltage range of 0.8 to 1.8 V and a scan rate of 5 mV s^{-1} in 1.0 M KOH.

Electrochemical in-situ Raman spectra measurements

The in-situ Raman spectroscopy experiments were performed using a Raman spectrometer (InVia Qontor, Renishaw) equipped with an in-situ test electrolytic cell (Gaoss Union C031-1). The laser excitation wavelength used was 532 nm and the exposure time was set to 10 min for each spectrum. The as-prepared catalyst, carbon rod and Ag/AgCl electrode served as the working electrode, counter electrode, and reference electrode, respectively. The evolution of catalyst was monitored by gathering Raman spectra at constant potential ranging from 1.0 to 1.8 V (*vs.* RHE).

2. Results and discussion

2.1. Synthesis and characterizations

The synthetic strategy and mechanism of 33% NiFeMOF/NFF nanosheet arrays are illustrated schematically in Figure 1a and Figure S1a. Thanks to the co-etching action of the solvent and ligand, NFF doubles as both the substrate and metal source for MOFs. Initially, the NFF's surface undergoes gradual oxidation by the solvent during the hydrothermal process, releasing Ni and Fe ions (Table S1). Subsequently, these ions aggregate with NDC^{2-}, resulting in the deposition of metal-organic hybrids on the NFF's surface. As the process unfolds, these hybrids start nucleating and growing (Figure S1c), culminating in the formation of cohesive nanosheet arrays (Figure S1d). A visual confirmation of MOF's growth on NFF is seen in the color shift

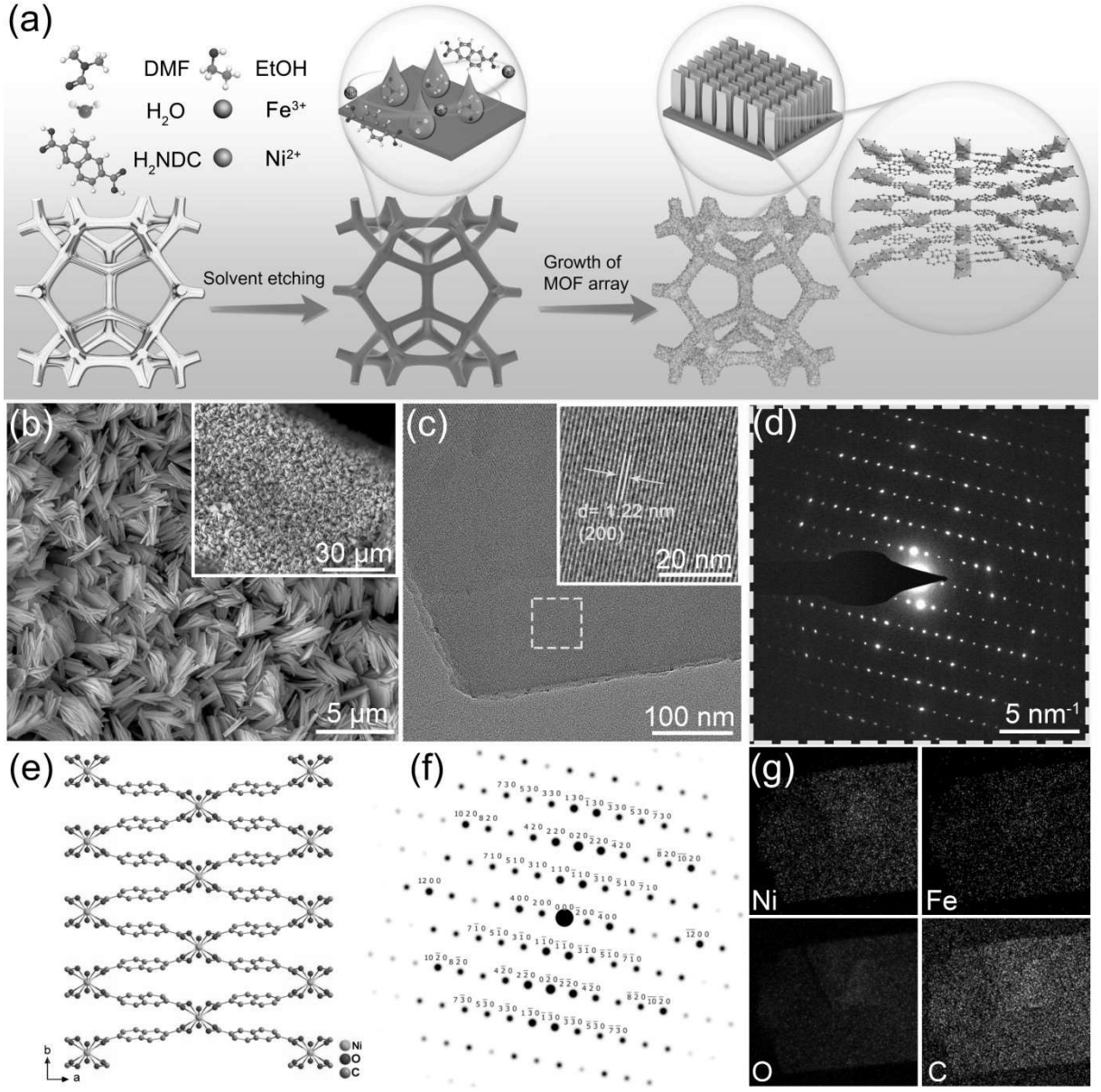

Figure 1. (a) Schematic illustration of the synthesis of NiFeMOF/NFF nanosheet arrays. (b) SEM image, (c) TEM and HRTEM images, (d) experimental SAED pattern obtained from the region in (c), (e) crystal structure, (f) simulated SAED pattern projected along the (001) zone axis, and (g) corresponding EDX elemental mappings of 33% NiFeMOF/NFF.

of NFF from silvery-white to a shade of brownish-yellow (Figure S2). As a comparison, NiMOF/NF and FeMOF/IF were prepared by the same method with NF and IF as substrate and metal source, respectively, and the surface of the catalysts shows grey and brown color.

X-ray diffraction (XRD) was employed to elucidate the crystal structure of the catalyst. The diffraction patterns observed for NiFeMOF/NFF, NiMOF/NF, and FeMOF/IF reveal identical peak patterns (Figure S3a), which align with MOF's known structural attributes (CCDC: 847283).[10] The distinct peaks located at 8.0° and 15.1° correspond to the (200) and (400) MOF planes, respectively. Meanwhile, pronounced peaks around 45° and 52.3° are indicative of the metallic Ni originating from NNF (PDF#04-0850), confirming successful NiFeMOF/NFF synthesis. To further validate this, Raman spectroscopy was used (Figure S3b). The recorded Raman spectra show three characteristic peaks at 853, 1120, and 1240 cm^{-1} corresponding to the bending vibrations of the C–H bond in the aromatic ring.[11] Additionally, peaks at 782 and 1631 cm^{-1} are representative of the stretching vibrations of the C–H and C–C bonds in the aromatic ring, respectively.[12] Notably, variations in the ethanol solvent ratios have no discernible impact on the MOF structure. Consequently, the consistency of the Raman spectra and XRD analysis results further confirms the successful synthesis of the MOF catalyst.

The morphological and microstructural characterization of the prepared 33% NiFeMOF/NFF was undertaken using scanning electron microscopy (SEM) and transmission electron

microscopy (TEM). The SEM image displays that uniform nanosheets grow on the surface of the NFF backbone (Figure 1b). Compared to disordered and stacked MOF nanomaterials, the 33% NiFeMOF/NFF's interlinked nanosheet arrangement offers numerous electrochemically active sites, promotes electrolyte permeation, and ensures robust mechanical durability, which is pivotal for optimizing catalytic activity.[13] Remarkably, the thickness of MOF nanosheets can be effectively regulated by altering the proportion of ethanol solvent (Figure S4). In the absence of ethanol, the MOF assumes a compact nanoplate form. However, increasing ethanol concentrations from 0% to 17%, 33%, 50%, and 67% see the MOF nanosheets' thickness gradually reduce to about 61 nm, 44 nm, 36 nm, and 15 nm, in that order (Figure S5). This hints at ethanol's influential role in mediating the MOF crystal's surface during its growth phase. Notably, the ICP results showed that the ethanol solvent ratios did not have a significant effect on the Ni/Fe ratio of NiFeMOF (Table S2).

As depicted in Figure 1c, the TEM image exhibits the smooth and flat surface of the 33% NiFeMOF/NFF nanosheets. The high-resolution TEM (HRTEM) displays distinct lattice fringes with an interplanar spacing of 1.22 nm, which is assigned to the (200) planes of the MOF. Moreover, the selected area electron diffraction (SAED) pattern shows prominent Bragg reflection points (Figure 1d). Notably, these dots are in perfect harmony with the modeled results acquired from the crystal structure's (001) zone axis (Figure 1e–f), indicating the exceptionally high crystallinity of the 33% NiFeMOF/NFF. Energy dispersive X-ray (EDX) elemental mapping was employed to assess the elemental distribution atop the 33% NiFeMOF/NFF. The findings confirm an even spread of Ni, Fe, C, and O elements across the nanosheet's surface (Figure 1g). For a point of reference, NiMOF/NF's morphology and structure were similarly probed. Both SEM and TEM images reveal the nanosheet-like configuration of NiMOF/NF (Figure S6a–b). As displayed in Figure S6c, the SAED pattern implies that the crystallinity of NiMOF/NF is comparable to that of 33% NiFeMOF/NFF. Furthermore, EDX analysis affirms that the Ni, C, and O elements are distributed uniformly in NiMOF/NF (Figure S6d), signifying the successful synthesis of isostructural MOFs with high crystallinity and phase purity.

X-ray photoelectron spectroscopy (XPS) was employed to discern the surface composition and electronic states of 33% NiFeMOF/NFF, NiMOF/NF, and FeMOF/IF. The XPS survey spectra (Figure S7) confirm the presence of Ni (Fe), O, and C elements in the respective samples, consistent with EDX results. The high-resolution XPS spectra of the C 1s region (Figure 2a) reveal three peaks at 284.8, 285.8, and 288.5 eV, corresponding to the C–C/C=C, C–O, and C=O bonds, respectively.[14] The O 1s XPS spectra can be deconvoluted into three peaks at 533.0, 531.7, and 530.6 eV, reflecting adsorbed water (H_2O_{ads}), C–O, and metal–oxygen (M–O) bonds, respectively (Figure 2b).[15] In the Ni 2p high-resolution spectra (Figure 2c), the characteristic peaks at approximately 856.2 and 874.0 eV correspond to the Ni^{2+} state.[16] Whereas, the weak peak at 853.0 eV can be attributed to the Ni^0 state in the NFF substrate.[17] In the Fe 2p XPS spectra (Figure 2d), the peaks located at 711.0 and 723.9 eV can be assigned to Fe $2p_{3/2}$ and Fe $2p_{1/2}$ of the Fe^{3+} state.[18] Notably, the Ni 2p peak position for 33% NiFeMOF/NFF exhibits a positive shift (~0.15 eV) compared to NiMOF/NF, whereas a negative binding energy shift (~0.13 eV) is evident for Fe 2p in 33% NiFeMOF/NFF compared with FeMOF/IF. The shifts in binding energies further demonstrate that there is an intense

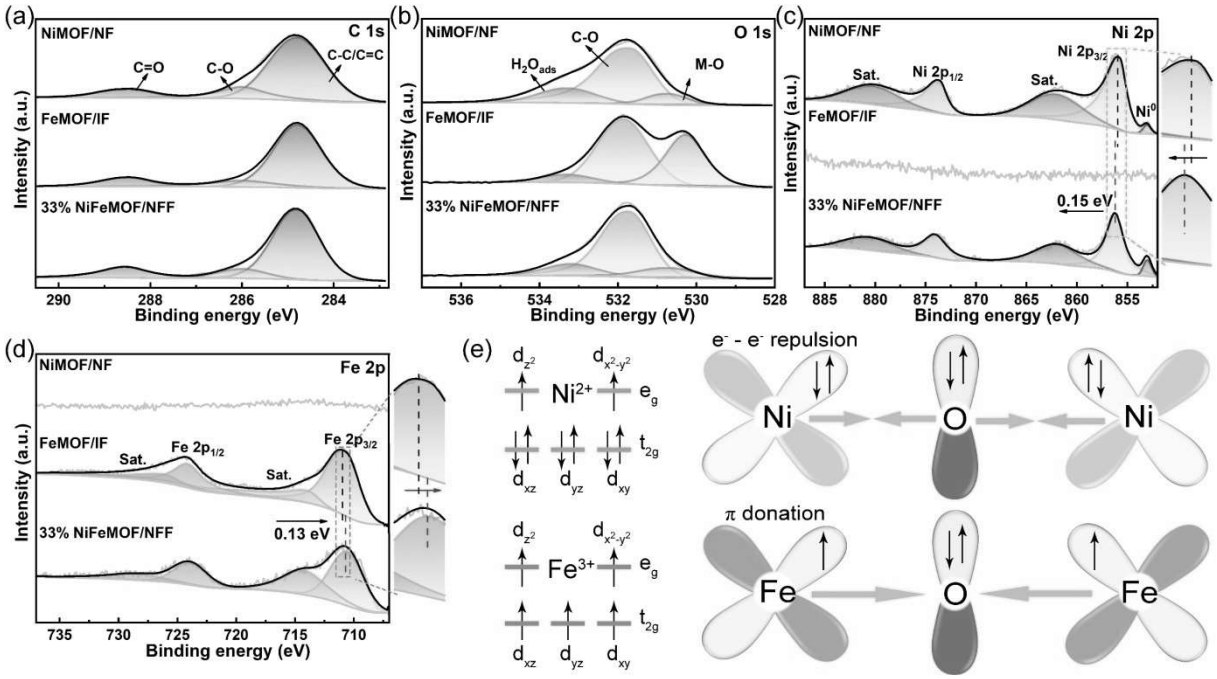

Figure 2. High-resolution XPS spectra of (a) C 1s, (b) O 1s, (c) Ni 2p, and (d) Fe 2p for NiMOF/NF, FeMOF/IF and 33% NiFeMOF/NFF. (e) Schematic representation of the electronic coupling between Ni and Fe.

electronic interaction between Ni and Fe in 33% NiFeMOF/NFF, which is conducive to enhancing OER activity.[19]

The synergistic electronic interplay of Ni and Fe cations in 33% NiFeMOF/NFF was further analyzed by the valence electron structure of metal ions. As shown in Figure 2e, Ni^{2+} ($t_{2g}^6e_g^2$) possesses a fully occupied π-symmetric (t_{2g}) *d*-orbital, resulting in e^--e^- repulsion with the ligand-bridged oxygen.[20] In contrast, Fe^{3+} ($t_{2g}^3e_g^2$) in a high spin state exhibits three unpaired π-symmetric (t_{2g}) *d*-orbitals and demonstrates weak π-donation interaction with the ligand-bridged oxygen.[21] Consequently, with the formation of Ni–O–Fe bond, the electron-electron repulsion between Ni and O strengthens the π-donation energy of Fe–O under the coupling of Ni^{2+} and Fe^{3+}, thereby prompting the electron transfer from Ni^{2+} to Fe^{3+},[22] consistent with the XPS findings. Moreover, the incorporation of Fe effectively modulates the electronic configuration of the Ni site, fine-tuning the adsorption/desorption capacity of oxygen-rich intermediates.[23] Notably, Ni^{2+} with partially filled e_g orbitals preferentially forms appropriate bonds with the adsorbed oxygen species, which contributes to enhancing the OER activity and expediting the reaction rate.[24]

2.2. Electrocatalytic OER performance

The catalysts' electrochemical performance for the oxygen evolution reaction (OER) was gauged at ambient temperature using a three-electrode setup, employing a 1.0 M KOH solution as the electrolyte. All recorded potentials were referenced to the reversible hydrogen electrode (RHE). The linear sweep voltammetry (LSV) curves (Figure 3a) demonstrate that 33% NiFeMOF/NFF exhibits superior electrocatalytic OER activity, requiring only ultra-low overpotentials of 188 and 240 mV to achieve current densities of 10 and 100 mA cm^{-2}, respectively, which are superior to other control samples and RuO_2. To delve into the reaction dynamics, Tafel slopes were derived from reverse-scan LSV trajectories (Figure S8) to rule out the influence of oxidation peaks. As shown in Figure 3b, the Tafel slope of 33% NiFeMOF/NFF (31 mV dec^{-1}) is significantly lower than that of 0% NiFeMOF/NFF (44 mV dec^{-1}), 17% NiFeMOF/NFF (44 mV dec^{-1}), 50% NiFeMOF/NFF (35 mV dec^{-1}), 67% NiFeMOF/NFF (39 mV dec^{-1}), and NiMOF/NF (71 mV dec^{-1}). The lower Tafel slope indicates that 33% NiFeMOF/NFF possesses highly favorable OER reaction kinetics.[25] Impressively, the overpotential at 10 mA cm^{-2} (η_{10}) and Tafel slope of 33% NiFeMOF/NFF surpassed those of other reported high-performance OER catalysts (Figure 3c and Table S3). Furthermore, electrochemical impedance spectroscopy (EIS) was conducted to investigate the charge transport capacity of the catalysts (Figure 3d). The bimetallic MOFs have smaller semicircle diameters compared to NiMOF/NF and FeMOF/IF, implying the smaller charge transfer resistance (R_{ct}) of bimetallic MOFs. Particularly, 33% NiFeMOF/NFF stands out with an R_{ct} of a mere 1.45 Ω, manifesting that it has the fastest charge transfer rate, which helps to accelerate the reaction kinetics and enhance OER activity. This improvement can be attributed to the synergy effect between Ni and Fe, which optimizes the electronic spin structure of the Ni sites.[26]

The electrochemically active surface area (ECSA) of the catalysts was estimated by calculating the double-layer capacitance (C_{dl}) from the cyclic voltammetry (CV) curves at different scanning rates (Figure S9 and Figure 3e). Among the samples, the C_{dl} of 33% NiFeMOF/NFF is 8.4 mF cm^{-2}, second only to that of 67% NiFeMOF/NFF. This can be attributed to the fact that under the influence of 67% ethanol, the nanosheets are thinner and therefore have a greater electrochemically active surface

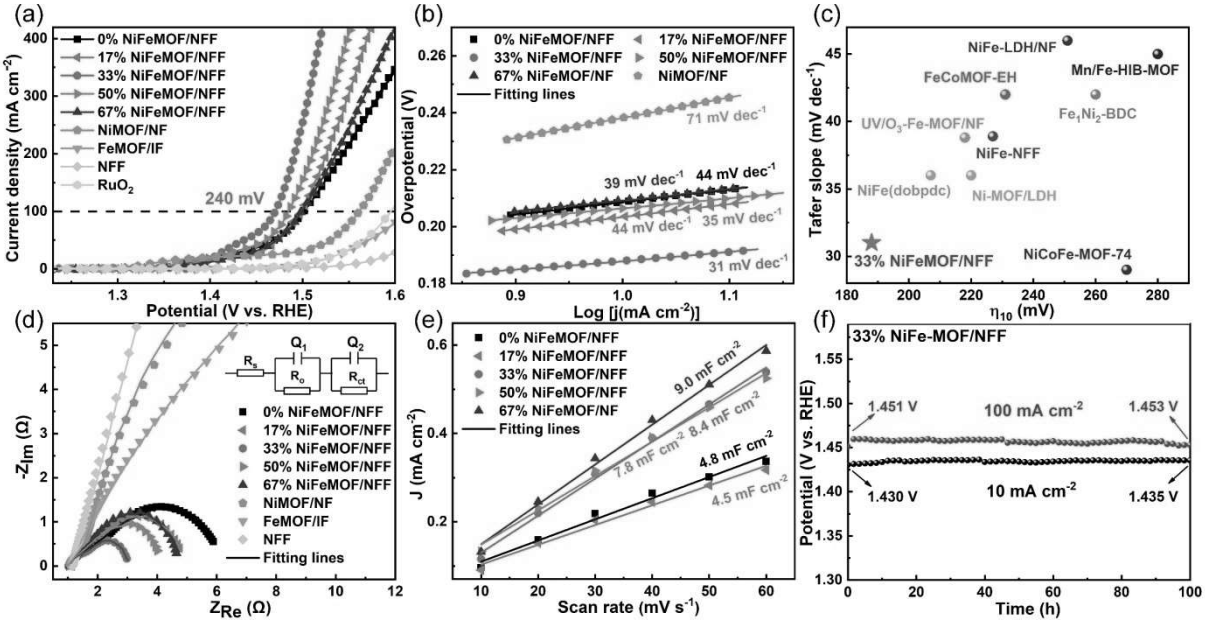

Figure 3. Electrocatalytic OER tests in 1.0 M KOH electrolyte using a three-electrode system for 0~67% NiFeMOF/NFF, NiMOF/NF, FeMOF/IF, and RuO_2/CFP. (a) LSV polarization curves, (b) Tafel slopes, (c) comparison of the overpotential at 10 mA cm^{-2} and Tafel slope with previously reported catalysts, (d) Nyquist plots, (e) double-layer capacitance (C_{dl}) plots, and (f) chronopotentiometry of 33% NiFeMOF/NFF at 10 and 100 mA cm^{-2}.

area. However, when the nanosheets are too thin, the material inevitably curls and is more prone to agglomeration and stacking due to the surface strain and high specific surface energy, resulting in suboptimal electrocatalytic performance.[27] In addition, the LSV polarization curves were normalized by ECSA to evaluate the intrinsic activity of the catalysts. As seen in Figure S10, 33% NiFeMOF/NFF displays a higher specific current density than other control samples, illustrating its higher intrinsic activity. Furthermore, 33% NiFeMOF/NFF demonstrates remarkable stability during long-term OER test. As shown in Figure 3f, there was no significant decline in overpotential after 100 h of continuous operation at current densities of 10 and 100 mA cm^{-2}.

2.3. Analyzing the dynamic transformation of catalysts during the OER process

To assess the catalysts' structural evolution following the OER reaction, post-reaction catalysts were scrutinized in greater detail. SEM and TEM images (Figure S11a–b) showed that 33% NiFeMOF/NFF nanosheet arrays underwent a large morphological change, exhibiting a rough honeycomb porous nanosheet structure after OER electrocatalysis. Notably, the SAED image (Figure S11c) shows that diffraction points belonging to MOF are partially preserved and can be attributed to the (220), (200), and (020) crystal planes, whereas the newly generated diffuse diffraction rings can be attributed to the (110) and (010) crystal planes of NiFeOOH (PDF# 18-0639). This observation suggests that partial MOF is reconstructed into NiFeOOH after the OER reaction process, resulting in the formation of 33% NiFeMOF/NiFeOOH complex. The corresponding EDX mappings show the uniform distribution of Ni, Fe, C, and O in 33% NiFeMOF/NiFeOOH (Figure S11d). As illustrated in Figure S12, the post-electrochemical reaction XRD patterns reveal that the characteristic MOF peaks are partially preserved, while the additional peaks can be attributed to NiFeOOH, further corroborating the aforementioned characterization.

A deeper dive via high-resolution XPS was undertaken to demystify the MOF's phase transition post-OER (Figure S13). In the Ni 2p XPS spectra of post-OER 33% NiFeMOF/NFF, the Ni^{2+} states (856.4 and 874.0 eV) are still present and form Ni^{3+} peaks at 862.0 and 876.4 eV attributed to NiOOH species.[28] Notably, a positive 0.1 eV shift is evident in the characteristic Ni $2p_{3/2}$ peak. In parallel, the Fe 2p spectra, after the OER assay, remain relatively unchanged, though the Fe $2p_{3/2}$ peak migrates towards a higher binding energy. These results suggest that Ni and Fe undergo a phase transition, leading to the formation of highly valent active species during electrocatalysis, which is consistent with previous characterizations. Importantly, the generation of highly valent reactive species leads to the alteration of the local electronic structure and facilitates partial electron transfer at the Ni site.[29] This is essential for facilitating deprotonation of adsorbates and accelerating electron transfer between surface cations and reaction intermediates.[30]

To further probe the MOF's structural transformation during electrocatalysis, in situ Raman measurements were implemented (Figure 4a). Figure 4b outlines the in situ Raman spectra

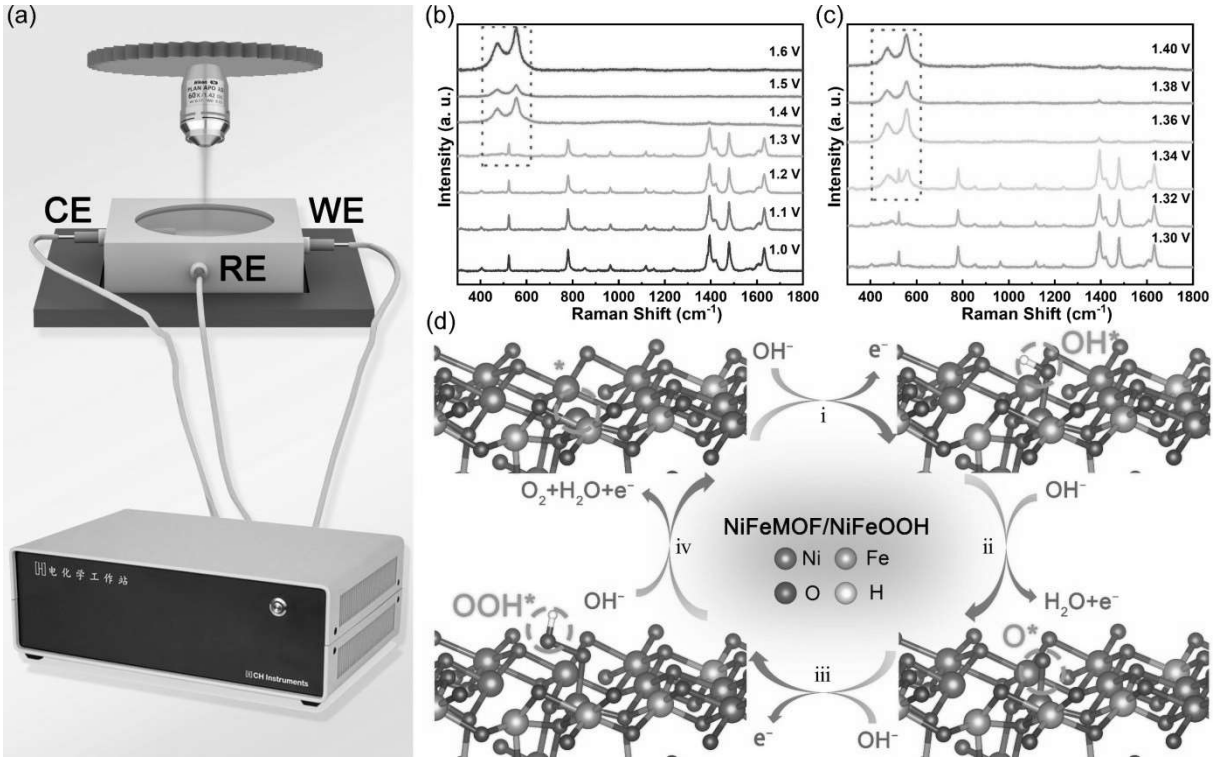

Figure 4. (a) In situ Raman instrument scheme. Electrochemical in situ Raman spectra of (b) 33% NiFeMOF/NFF in the potential range of 1.0–1.8 V (*vs.* RHE), and (c) in the potential range of 1.30–1.40 V (*vs.* RHE), respectively. (d) OER mechanistic illustration of 33% NiFeMOF/NiFeOOH.

across a potential spectrum from 1.0 to 1.8 V (*vs.* RHE) with intervals of 0.1 V. Notably, the Raman spectra do not change significantly at potentials below 1.3 V (*vs.* RHE). However, when the potential reaches 1.4 V (*vs.* RHE), the characteristic peaks of MOF diminish noticeably, while two new peaks emerge at approximately 474 and 554 cm^{-1}, corresponding to the E_g bending and A_{1g} stretching vibrations of Ni/Fe–O in NiFeOOH.[31] The in situ Raman spectra of NiMOF/NF are similar to those of 33% NiFeMOF/NFF and exhibit a phase transition process to the NiOOH (Figure S14a). Consequently, the structural evolution of 33% NiFeMOF/NFF and NiMOF/NF were further investigated in the potential interval from 1.3 V to 1.4 V (*vs.* RHE) (Figure 4c and S14b). Interestingly, the 33% NiFeMOF/NFF Raman spectra already exhibit the characteristic peaks of NiFeOOH at 1.34 V (*vs.* RHE), whereas the NiMOF/NF Raman spectra display no significant changes. The NiOOH characteristic peaks in the NiMOF/NF Raman spectra become visible when the potential reaches 1.36 V (*vs.* RHE). Therefore, 33% NiFeMOF/NFF has a lower transition potential to MOOH compared to NiMOF/NF. This disparity can be attributed to the strong synergistic interaction between Fe and Ni species, which effectively reduces the oxidation potential required to form highly valent active species,[32] thus improving the OER performance of 33% NiFeMOF/NFF.

To elucidate the catalytic mechanism, the structural model of NiFeMOF/NiFeOOH was simulated and the Ni atoms on the surface of NiFeOOH served as active sites (Figure S15). The proposed catalytic mechanism is as follows (Figure 4d): Initially, OH^- in the electrolyte absorbs on the Ni sites to form the Ni–OH group (Step 1). Subsequently, the first deprotonation of the Ni–OH group occurs to generate the Ni–O group and H_2O (Step 2). As the reaction progresses, the Ni–O group combines with OH^- to produce the superoxide species Ni–OOH (Step 3). Finally, the Ni–OOH reacts with the OH^- and undergoes deprotonation, thereby generating O_2 and H_2O (Step 4).[25] The spin state of Ni^{3+} ions was examined to clarify the reasons for the remarkable catalytic activity of 33% NiFeMOF/NFF. The excellent electrocatalytic activity can be attributed to the formation of more Ni^{3+}, whose electronic configuration ($t_{2g}^6e_g^1$) is closer to the optimal $e_g^{1.2}$ electronic configuration than that of Ni^{2+} ($t_{2g}^6e_g^2$)[20] because the filling of e_g-orbitals is more suitable for catalysis. Specifically, the σ-bonding e_g orbital overlaps more strongly with the oxygen-related adsorbate than the *p*-bonding t_{2g} orbital, which is conducive to facilitating the electron transfer between the surface cation and the adsorbed reaction intermediates.[30b] Moreover, this enhanced orbital overlap results in increased covalence of the transition metal–oxygen bond (Ni–O), consequently accelerating the OER kinetics.[33]

2.4. Overall water splitting analysis

Considering the impressive OER performance and robust stability of the 33% NiFeMOF/NFF catalyst, a two-electrode system (33% NiFeMOF/$NFF^{(+)}$||$Pt/C^{(-)}$) was constructed by employing 33% NiFeMOF/NFF as the anode and Pt/C as the cathode, respectively, in 1.0 M KOH for the overall water splitting. For comparison, $RuO_2^{(+)}$||$Pt/C^{(-)}$ was also assembled and tested under the same conditions (Figure 5a). As delineated in Figure 5b, the 33% NiFeMOF/$NFF^{(+)}$||$Pt/C^{(-)}$ showcases commendable water-splitting efficiency, demanding only nominal cell voltages of 1.55 V and 1.83 V to achieve current densities of 10 and 100 mA cm^{-2}, respectively, which much better than those of benchmark $RuO_2^{(+)}$||$Pt/C^{(-)}$ (Figure S16). Compared with previously reported advanced MOF electrocatalysts, the 33% NiFeMOF/NFF performs superior water splitting performance (Figure 5c and Table S4). Moreover, the long-term durability of 33% NiFeMOF/$NFF^{(+)}$||$Pt/C^{(-)}$ was assessed through chronopotential measurements (Figure 5d). The outcomes indicate the robustness of the 33% NiFeMOF/$NFF^{(+)}$||$Pt/C^{(-)}$ system, confirming its ability to sustain operations over 100 hours at a consistent current density of 100 mA cm^{-2}, thus underscoring its remarkable stability.

3. Conclusions

In summary, a versatile and simple self-etching assembly strategy was developed for the synthesis of metal-based MOF catalysts. The experimental investigations demonstrate that it is a reliable method to optimize the catalytic activity by adjusting the spin density of the active site in the MOF structure. The prepared 33% NiFe–MOF/NFF nanosheet arrays have fast charge transfer ability and good mechanical stability. And 33% NiFeMOF/NFF displays impressive OER activity and long-term stability. Additionally, when applied in a two-electrode system, it performs outstanding overall water splitting that far exceeds that of the benchmark electrolyzer. Electrochemical in-situ Raman spectroscopy and ex-situ structure characterization indicate that 33% NiFeMOF/NiFeOOH is the actual active species. Importantly, its excellent activity is due to the electronic coupling between Fe and Ni species. This work provides a promising method for the design of high-performance OER electrocatalysts.

Acknowledgements

This work has been supported by the National Natural Science Foundation of China (no. 21965005, 22068008, 52363028), Natural Science Foundation of Guangxi Province (2021GXNSFAA076001), and Guangxi Technology Base and Talent Subject (GUIKE AD23023004, GUIKE AD20297039).

Conflict of Interests

The authors declare that they have no known competing financial interests or personal relationships that could have appeared to influence the work reported in this paper.

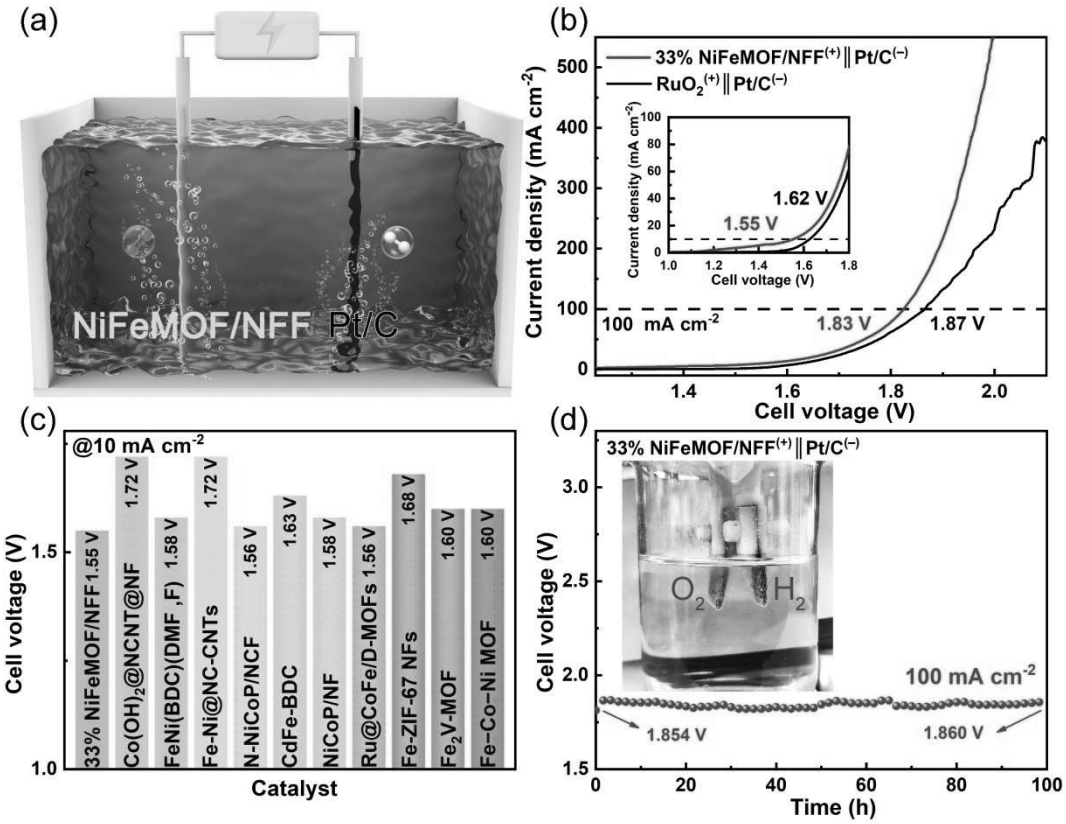

Figure 5. (a) Schematic diagram of overall water splitting in the two-electrode system. (b) Polarization curves of 33% NiFeMOF/NFF$^{(+)}$||Pt/C$^{(-)}$ and $RuO_2^{(+)}$||Pt/C$^{(-)}$ for overall water splitting in 1.0 M KOH. (c) Comparison of the cell voltage at 10 mA cm^{-2} with previously reported catalysts in 1.0 M KOH. (d) Chronopotentiometry test at 100 mA cm^{-2}.

Data Availability Statement

Research data are not shared.

Keywords: metal-organic frameworks · self-etching assembly · oxygen evolution · overall water splitting

[1] a) Y. Z. Wang, M. Yang, Y.-M. Ding, N.-W. Li, L. Yu, *Adv. Funct. Mater.* **2022**, *32*, 2108681; b) Z.-Y. Yu, Y. Duan, X.-Y. Feng, X. Yu, M.-R. Gao, S.-H. Yu, *Adv. Mater.* **2021**, *33*, 2007100; c) X. Ren, T. Wu, Y. Sun, Y. Li, G. Xian, X. Liu, C. Shen, J. Gracia, H.-J. Gao, H. Yang, Z. J. Xu, *Nat. Commun.* **2021**, *12*, 2608; d) J. Hao, J. Liu, D. Wu, M. Chen, Y. Liang, Q. Wang, L. Wang, X.-Z. Fu, J.-L. Luo, *Appl. Catal. B* **2021**, *281*, 119510.

[2] a) R. R. Rao, S. Corby, A. Bucci, M. García-Tecedor, C. A. Mesa, J. Rossmeisl, S. Giménez, J. Lloret-Fillol, I. E. L. Stephens, J. R. Durrant, *J. Am. Chem. Soc.* **2022**, *144*, 7622–7633; b) X. L. Wang, L. Z. Dong, M. Qiao, Y. J. Tang, J. Liu, Y. Li, S. L. Li, J. X. Su, Y. Q. Lan, *Angew. Chem. Int. Ed.* **2018**, *57*, 9660–9664; c) P. Wang, M. Yan, J. Meng, G. Jiang, L. Qu, X. Pan, J. Z. Liu, L. Mai, *Nat. Commun.* **2017**, *8*, 645.

[3] a) M. Singh, T. T. Nguyen, M. A. P, Q. P. Ngo, D. H. Kim, N. H. Kim, J. H. Lee, *Small* **2023**, *19*, 2206726; b) W. Zhu, X. Yue, W. Zhang, S. Yu, Y. Zhang, J. Wang, J. Wang, *Chem. Commun.* **2016**, *52*, 1486–1489.

[4] a) Y. Yang, S. Wei, Y. Li, D. Guo, H. Liu, L. Liu, *Appl. Catal. B* **2022**, *314*, 121491; b) Y. Wu, G.-D. Li, Y. Liu, L. Yang, X. Lian, T. Asefa, X. Zou, *Adv. Funct. Mater.* **2016**, *26*, 4839–4847.

[5] a) X.-K. Wan, H. B. Wu, B. Y. Guan, D. Luan, X. W. Lou, *Adv. Mater.* **2020**, *32*, 1901349; b) Y. Rao, Y. Wang, H. Ning, P. Li, M. Wu, *ACS Appl. Mater. Interfaces* **2016**, *8*, 33601–33607.

[6] a) J. Huang, Y. Li, R.-K. Huang, C.-T. He, L. Gong, Q. Hu, L. Wang, Y.-T. Xu, X.-Y. Tian, S.-Y. Liu, Z.-M. Ye, F. Wang, D.-D. Zhou, W.-X. Zhang, J.-P. Zhang, *Angew. Chem. Int. Ed.* **2018**, *57*, 4632–4636; b) H. Wu, J. Wang, W. Jin, Z. Wu, *Nanoscale* **2020**, *12*, 18497–18522; c) S. Li, Y. Gao, N. Li, L. Ge, X. Bu, P. Feng, *Energy Environ. Sci.* **2021**, *14*, 1897–1927; d) L. Jiao, Y. Wang, H.-L. Jiang, Q. Xu, *Adv. Mater.* **2018**, *30*, 1703663.

[7] C. Cao, D.-D. Ma, Q. Xu, X.-T. Wu, Q.-L. Zhu, *Adv. Funct. Mater.* **2019**, *29*, 1807418.

[8] a) F. Wu, X. Guo, G. Hao, Y. Hu, W. Jiang, *Nanoscale* **2019**, *11*, 14785–14792; b) L. Ye, J. Wang, Y. Zhang, M. Zhang, X. Jing, Y. Gong, *Appl. Surf. Sci.* **2021**, *556*, 149781; c) F. Shahbazi Farahani, M. S. Rahmanifar, A. Noori, M. F. El-Kady, N. Hassani, M. Neek-Amal, R. B. Kaner, M. F. Mousavi, *J. Am. Chem. Soc.* **2022**, *144*, 3411–3428.

[9] a) J. Wang, Y. Jiang, C. Liu, Y. Wu, B. Liu, W. Jiang, H. Li, G. Che, *J. Colloid Interface Sci.* **2022**, *614*, 532–537; b) J. Yu, Y. Cao, Q. Liu, Y. Luo, Y. Liu, X. Shi, A. M. Asiri, T. Li, X. Sun, *ChemNanoMat* **2021**, *7*, 906–909; c) Z. Li, J. Yang, Z. Chen, C. Zheng, L. Q. Wei, Y. Yan, H. Hu, M. Wu, Z. Hu, *Adv. Funct. Mater.* **2021**, *31*, 2008822.

[10] Y.-Y. Liu, K. Leus, M. Grzywa, D. Weinberger, K. Strubbe, H. Vrielinck, R. Van Deun, D. Volkmer, V. Van Speybroeck, P. Van Der Voort, *Eur. J. Inorg. Chem.* **2012**, *2012*, 2819–2827.

[11] Q. Li, X. Wang, N. Yang, F. He, Y. Yang, B. Wu, J. Chu, A. Zhou, S. Xiong, *Z. Anorg. Allg. Chem.* **2019**, *645*, 1022–1030.

[12] H. Zhao, L. Zhang, L. Dai, F. Yao, Y. Huang, J. Deng, Y. Fu, J. Zhu, J. Sun, *Appl. Surf. Sci.* **2022**, *592*, 153252.

[13] a) W. Li, S. Watzele, H. A. El-Sayed, Y. Liang, G. Kieslich, A. S. Bandarenka, K. Rodewald, B. Rieger, R. A. Fischer, *J. Am. Chem. Soc.* **2019**, *141*, 5926–5933; b) L. Xiao, Z. Wang, J. Guan, *Coord. Chem. Rev.* **2022**, *472*, 214777.

[14] Y. Jiang, T.-Y. Chen, J.-L. Chen, Y. Liu, X. Yuan, J. Yan, Q. Sun, Z. Xu, D. Zhang, X. Wang, C. Meng, X. Guo, L. Ren, L. Liu, R. Y.-Y. Lin, *Adv. Mater.* **2024**, *36*, 2306910.

[15] Y. Tang, Q. Liu, L. Dong, H. B. Wu, X.-Y. Yu, *Appl. Catal. B* **2020**, *266*, 118627.

[16] a) D. Xiong, M. Gu, C. Chen, C. Lu, F.-Y. Yi, X. Ma, *Chem. Eng. J.* **2021**, *404*, 127111; b) W. Chen, Y. Zhang, G. Chen, R. Huang, Y. Wu, Y. Zhou, Y. Hu, K. Ostrikov, *J. Colloid Interface Sci.* **2020**, *560*, 426–435.

[17] a) S. Anantharaj, J. Kennedy, S. Kundu, *ACS Appl. Mater. Interfaces* **2017**, *9*, 8714–8728; b) C. Dong, T. Kou, H. Gao, Z. Peng, Z. Zhang, *Adv. Energy Mater.* **2018**, *8*, 1701347.
[18] B. Zhang, C. Xiao, S. Xie, J. Liang, X. Chen, Y. Tang, *Chem. Mater.* **2016**, *28*, 6934–6941.
[19] J. Su, R. Ge, K. Jiang, Y. Dong, F. Hao, Z. Tian, G. Chen, L. Chen, *Adv. Mater.* **2018**, *30*, 1801351.
[20] Y. Zhai, X. Ren, Y. Sun, D. Li, B. Wang, S. Liu, *Appl. Catal. B* **2023**, *323*, 122091.
[21] J. Jiang, F. Sun, S. Zhou, W. Hu, H. Zhang, J. Dong, Z. Jiang, J. Zhao, J. Li, W. Yan, M. Wang, *Nat. Commun.* **2018**, *9*, 2885.
[22] C.-F. Li, J.-W. Zhao, L.-J. Xie, J.-Q. Wu, Q. Ren, Y. Wang, G.-R. Li, *Angew. Chem. Int. Ed.* **2021**, *60*, 18129–18137.
[23] B. Fei, Z. Chen, J. Liu, H. Xu, X. Yan, H. Qing, M. Chen, R. Wu, *Adv. Energy Mater.* **2020**, *10*, 2001963.
[24] C.-F. Li, L.-J. Xie, J.-W. Zhao, L.-F. Gu, H.-B. Tang, L. Zheng, G.-R. Li, *Angew. Chem. Int. Ed.* **2022**, *61*, e202116934.
[25] Y. Chen, J. Wang, Z. Yu, Y. Hou, R. Jiang, M. Wang, J. Huang, J. Chen, Y. Zhang, H. Zhu, *Appl. Catal. B* **2022**, *307*, 121151.
[26] Y. Li, M. Yuan, H. Yang, K. Shi, Z. Sun, H. Li, C. Nan, G. Sun, *Appl. Catal. B* **2023**, *323*, 122167.
[27] a) C. Spöri, J. T. H. Kwan, A. Bonakdarpour, D. P. Wilkinson, P. Strasser, *Angew. Chem. Int. Ed.* **2017**, *56*, 5994–6021; b) H. Feng, Z. Xu, L. Wang, Y. Yu, D. Mitchell, D. Cui, X. Xu, J. Shi, T. Sannomiya, Y. Du, W. Hao, S. X. Dou, *ACS Appl. Mater. Interfaces* **2015**, *7*, 27592–27596.
[28] J. Liu, J. Yang, Y. Song, J. Sun, Y. Tian, Q. Chen, X. Zhang, L. Zhang, *J. Colloid Interface Sci.* **2023**, *643*, 17–25.
[29] M. W. Louie, A. T. Bell, *J. Am. Chem. Soc.* **2013**, *135*, 12329–12337.
[30] a) W. Cheng, X. Zhao, H. Su, F. Tang, W. Che, H. Zhang, Q. Liu, *Nat. Energy* **2019**, *4*, 115–122; b) Y. Wang, M. Qiao, Y. Li, S. Wang, *Small* **2018**, *14*, 1800136; c) H.-Y. Wang, Y.-Y. Hsu, R. Chen, T.-S. Chan, H. M. Chen, B. Liu, *Adv. Energy Mater.* **2015**, *5*, 1500091.
[31] J. Huang, Y. Li, Y. Zhang, G. Rao, C. Wu, Y. Hu, X. Wang, R. Lu, Y. Li, J. Xiong, *Angew. Chem. Int. Ed.* **2019**, *58*, 17458–17464.
[32] W. Wu, Z. Gao, Q. Li, Z. Wang, S. Liu, H. Wu, Y. Zhao, Y. Jiao, X. Zhao, *J. Energy Chem.* **2022**, *74*, 404–411.
[33] Z. Xu, Y. Ying, G. Zhang, K. Li, Y. Liu, N. Fu, X. Guo, F. Yu, H. Huang, *J. Mater. Chem. A* **2020**, *8*, 26130–26138.

Manuscript received: November 6, 2023
Revised manuscript received: February 7, 2024
Accepted manuscript online: February 8, 2024
Version of record online: February 26, 2024